Laser & Photonics Reviews

LASER & PHOTONICS REVIEWS

www.lpr-journal.org

RESEARCH ARTICLE OPEN ACCESS

Near-Infrared Polarimetric Imaging With Nonlinear Flat-Optics

Evgenii Menshikov[1] | Marco A. López Sánchez[2] | Paolo Franceschini[1,3] | Andrea Tognazzi[3,4] | Domenico de Ceglia[1,3] | Kristina Frizyuk[5] | Costantino De Angelis[1,3]

[1]Università degli studi di Brescia, Brescia, Italy | [2]Photonics Research Group, Ghent University-IMEC, Ghent, Belgium | [3]Istituto Nazionale di Ottica - Consiglio Nazionale delle Ricerche (INO-CNR), Brescia, Italy | [4]Università degli studi di Palermo, Palermo, Italy | [5]Karlsruhe Institute of Technology, Karlsruhe, Germany

Correspondence: Costantino De Angelis (costantino.deangelis@unibs.it)

Received: 26 December 2025 | **Revised:** 19 April 2026 | **Accepted:** 7 May 2026

Keywords: nonlinear circular dichroism | nonlinear optics | polarimetry | second harmonic generation

ABSTRACT

A compact and broadband polarimetric imaging platform is presented, based on second-harmonic generation (SHG) in nonlinear flat-optics. The system employs periodic all-dielectric AlGaAs gratings to induce polarization-dependent SH emission, enabling pixel by pixel direct retrieval of the full Stokes vector from an input intensity distribution in the near-infrared range. By engineering the geometry and orientation of the polarimetric units, sensitivity to linear and circular polarization components is achieved. A superpixel design comprising four polarimetric structures allows accurate reconstruction of the polarization state without moving parts or sequential measurements. This approach offers a scalable, passive, and cost-effective solution for polarimetric imaging, particularly suited for near-infrared applications.

1 | Introduction

An electromagnetic (EM) monochromatic plane wave has four degrees of freedom, namely the amplitude A, the phase ϕ, the polarization orientation ψ, and ellipticity χ [1]. In fact, the parameters ψ and χ describe the so-called State of Polarization (SoP) and specify the properties of the electric field oscillations in the plane perpendicular to the propagation direction. This intrinsic property of radiation plays a crucial role in both the fundamental understanding of light features and in a variety of applications [2]. Indeed, the measurements and the analysis of the SoP (i.e., polarimetry [3]) is of paramount importance in various fields, such as astronomy [4], remote sensing [3], quantum optics [5], and biology [6]. In particular, imaging polarimetry (the technique aiming at mapping the SoP across a vast scene of interest), given its ability to analyze spatially varying light beams, allows one to retrieve information about the shape [7–9] and arrangement [10, 11] of the reflecting structures, the orientation of light emitters [12–14], or the optical activity of various materials [15]. Therefore, in the last decades, several methods have been developed to measure the SoP in an extended scene [3].

A widely spread representation of the SoP is given by the Stokes vector formalism [1, 16]. Within this framework, the SoP of an arbitrary polarized wavefront is represented as a four-element vector, i.e., the Stokes vector, $\mathbf{S} = (S_0, S_1, S_2, S_3)$. Given a Cartesian reference frame xyz, with z being the propagation direction, the vector components are defined as $S_0 = I$, $S_1 = I_x - I_y$, $S_2 = I_{L+45} - I_{L-45}$, and $S_3 = I_{\mathrm{RCP}} - I_{\mathrm{LCP}}$. In the previous expressions, I is the total intensity of the light-field and the terms I_x, I_y, I_{L+45}, and I_{L-45} are the intensity of light in linear polarization component along the x (horizontal, H), y (vertical, V), $+45°$, and $-45°$ direction, respectively. The terms I_{RCP} and I_{LCP} denote the intensity of the right-hand (RCP) and left-hand (LCP) circularly polarized light, respectively. From a conceptual point

of view, the Stokes vector formalism allows to describe the SoP of the input light as the projection on three polarization basis sets: *i)* H/V (S_1), *ii)* ±45° (S_2), and *iii)* RCP/LCP (S_3). Practically, this means that the value of the components S_0, S_1, S_2, and S_3 can be directly determined by measuring the intensity (or power) in the different polarization bases. From an experimental point of view, this is a big advantage, since standard photodetectors operating at optical frequencies typically respond to changes in the intensity of the EM field (not to its phase).

A typical polarimetry assessment setup always contains two parts: the polarization analyzer and the detection system (electric readout). The light detector probes the output response (such as an optical signal or photocurrent) resulting from the interaction between the analyzer and the incident radiation with unknown SoP. In the traditional approach, the radiation under analysis propagates sequentially through rotating polarizing elements (optical analyzer) and the transmitted intensity is measured by a photodetector [16]. The SoP is thus determined from several (a minimum of four) intensity measurements by properly arranging the polarizing elements in front of the detector. This takes relatively long acquisition times and it is not capable to monitor transient events. Another method consists in performing parallel measurements by splitting the beam into several optical paths and using multiple polarizers and detectors [3, 17], but result in inherently complex and bulky systems. These limitations were alleviated with the development of integrated polarimetric devices employing variable liquid crystal retarders [18, 19]. These devices are designed to dynamically modulate the retardance values under an external voltage, allowing the full polarization state to be reconstructed from sequential measurements. More compact implementations include thin-film analyzers (micropolarizer gratings) [20, 21] and devices based on two-dimensional (2D) materials, exploiting their anisotropic absorption [22]. While both types of devices exhibit strong sensitivity to linear polarization, their response to circular components is usually absent or quite limited, requiring more advanced designs [23–25].

In the past decade, metasurfaces (optical elements composed of judiciously arranged nanoscatterers) have opened new avenues in the manipulation of light's amplitude, phase, and SoP [26–28]. Among a wide variety of applications, dielectric metasurfaces have been successfully employed also for imaging polarimetry [29–31]. In these devices, the extended wavefront impinges onto the polarimetric unit composed of an ordered array of unit elements with specific shapes and/or orientations. The individual polarimetric units (called super-pixels) comprise a set of optical metasurfaces, each one being designed to respond only to one of the three polarization basis (e.g., H/V, ±45°, or RCP/LCP) and it splits the two orthogonal states of polarization to different points on the detection plane. The determination of the Stokes parameters is achieved by measuring the intensity at image sensor pixels on the detector plane, corresponding to one single super-pixel on the analyzer plane. Further advances along this path are represented by the integration of a metasurface analyzer directly with a photodetector, enabling an extremely compact and self-contained polarimetric platform [32–34]. In this case, the individual super-pixel comprises a few sensing units (three or four depending on the implementations), whose output photocurrent depends on the SoP of the input light. The Stokes parameters are extracted by measuring the photocurrent levels from the various sensing units, each one addressing one specific polarization basis. Successful implementations of this working principle include, for example, integrated metasurface polarization filters [34], chiral plasmonic metasurfaces integrated with graphene–silicon photodetectors [32], or Weyl semimetal sensing units accompanied by integrated grating waveplates [33].

Here, we propose a novel method to determine the SoP of polarized light at fundamental frequency (FF) based on second-harmonic (SH) generation process in a nonlinear all-dielectric platform. We show that in specifically optimized periodic structures, the intensity of SH radiation depends on the SoP of the FF, allowing for full Stokes polarization retrieval. Namely, we show that polarization-dependent SH generation can be induced by grating units fabricated from [001]||z-oriented aluminum gallium arsenide (AlGaAs) thin film each featuring an identical, nonchiral geometry but differing in the bars orientation within the ⟨001⟩ plane of the crystalline lattice. To fully explain the process, we introduce an analytical description of the properties of the nonlinear radiation from the periodic polarimetric unit. Finally, we numerically demonstrate the capability of a four-unit super-pixel as polarization analyzer for imaging polarimetry. We show that the full set of Stokes parameters can be extracted from the intensity measurements of the SH radiation from individual scatterers using an image sensor placed at the detection plane. Our results indicate that nonlinear optics holds strong potential for developing broadband imaging polarimetry devices with low fabrication complexity suitable for near-IR operation.

2 | Theory and Modeling

Figure 1 illustrates the concept of a nonlinear all-dielectric polarimetric imaging device. The device consists of an array of polarimetric super-pixels, comprising four gratings made of a thin layer of nonlinear medium (AlGaAs) on a Al_2O_3 substrate, as shown in Figure 1a. The gratings have the same geometrical sizes, but are rotated at different angles β with respect to the crystalline lattice. Depending on the rotation angle, we denote them as U_L^x and U_R^x for the units rotated with respect to the x-axis, and U_L^y and U_R^y for those rotated with respect to the y-axis, where the R and L subscripts indicate the handedness that maximizes the SH signal. The units are illuminated from the substrate side and generate SH in the open 0 and ±1 diffraction orders in air (in the operating range 1450–1650 nm), as shown in the left panel of Figure 1b. Further, when referring to the SH signal, we mean total contribution from all diffraction orders. After nonlinear interaction, both the transmitted fundamental light (ω) and the generated SH signal (2ω) are collected with a lens (see Figure 1c). Next, the SH signal is relayed onto a CCD camera via a telescope system for analysis of the polarization dependent nonlinear response. The fundamental harmonic, which is only weakly influenced by its interaction with the units, can be redirected away from the main optical path using a dichroic mirror, which transmits the SH signal and reflects the pump.

Twist between the gratings and the lattice allowed us to achieve discrimination between the right and left-hand polarization states. Here we exploit the phenomenon of circular dichroism at second harmonic (SH-CD), or the sensitivity of the second-order

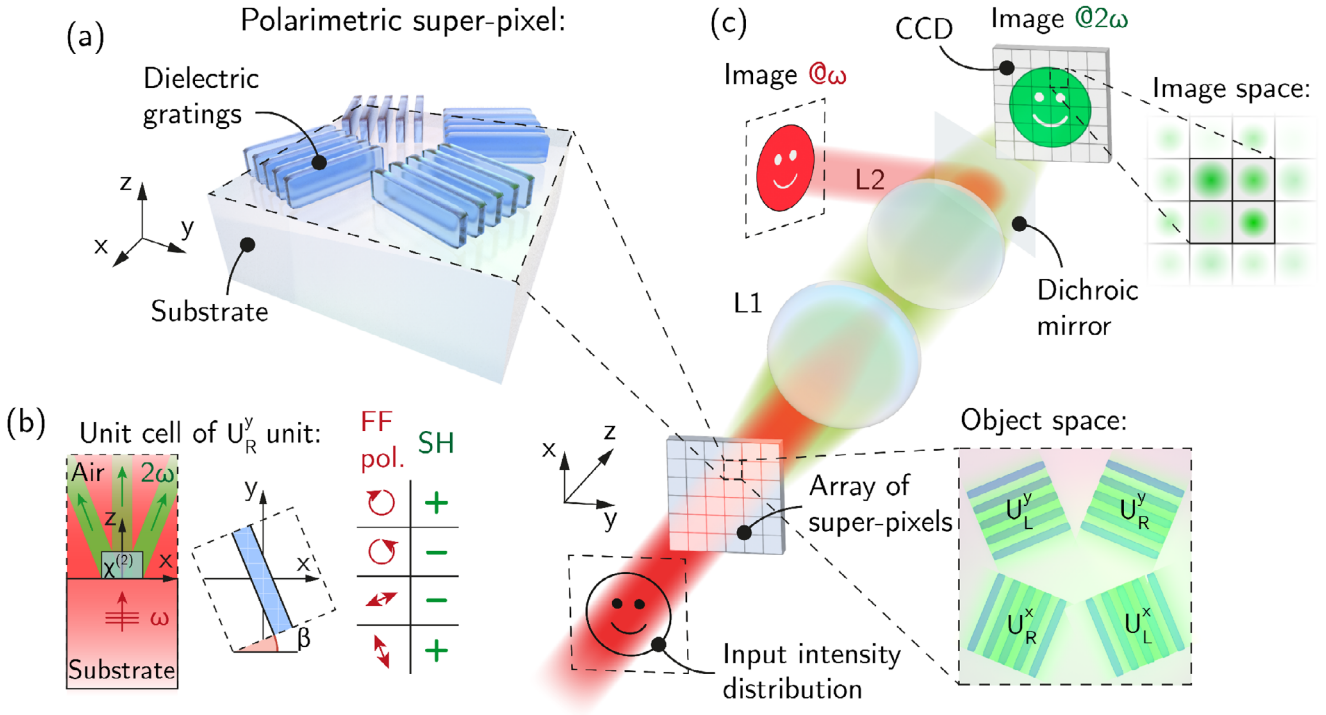

FIGURE 1 | Visualization of the nonlinear polarimetric device. (a) The polarimetric super-pixel consists of four all-dielectric gratings tilted by $\pm\pi/8$ ($\pm 22.5°$) with respect to the crystalline lattice of the AlGaAs film. (b) Under illumination by a pump irradiation, the fundamental field generates second harmonic signal in the $\chi^{(2)}$ layer, which is most prominent for RCP or linear input parallel to the grating bars, and negligible for the LCP or LP orthogonal to the bars. (c) SH response from the polarimetric units arranged in an array of super-pixels is relayed by the telescope formed by lenses L_1 and L_2 on the CCD, allowing for the imaging polarimetry.

nonlinear response to the handedness of the circular polarization [35], which quantitatively can be expressed through the ratio SH-CD = $(I^{2\omega}_{\mathrm{RCP}} - I^{2\omega}_{\mathrm{LCP}})/(I^{2\omega}_{\mathrm{RCP}} + I^{2\omega}_{\mathrm{LCP}})$ [36]. As we will show below, the symmetry of the nonlinear crystal and the structure give rise to particular angular terms in the dependence of SH power on the input polarization orientation angle, ψ, with their relative weights determined by the value of the SH-CD. We leverage this property to obtain strong SH contrast between RCP and LCP excitation and a distinct SH response for input fields oriented parallel or orthogonal to the grating bars, as schematically summarized in Figure 1b. Generally, the suggested units generate a SH response similar to the response of a rotated elliptical polarizer, allowing for polarimetric measurements using a set of units with identical geometries oriented differently in space [37].

The geometry of the device was optimized in COMSOL Multiphysics software to exhibit maximal SH circular dichroism (SH-CD = 0.981 with input at 1550 nm), resulting in a value of the SH linear dichroism of SH-LD = $(I^{2\omega}_{||} - I^{2\omega}_{\perp})/(I^{2\omega}_{||} + I^{2\omega}_{\perp}) = 0.956$ (see Section S1). The corresponding geometrical parameters are a bar width $w = 653$ nm, a period $\Lambda = 1316$ nm, and a height $h = 246$ nm. We find that the simultaneous maximization of LP and CD in our design leads to minor variations in the optimized geometrical parameters (see Section S2).

2.1 | Nonlinear Response of Polarimetric Units

Figure 2a shows the numerical simulation of the SH power emitted by the polarimetric units following FF excitation, whose polarization state traverses the entire Poincaré sphere. Here we utilize the formalism of a polarization ellipse SoP which is parametrized by the ellipticity angle $\chi \in [-\pi/4, \pi/4]$ and orientation angle $\psi \in [0, \pi]$ (see inset in Figure 2a). From the map of the polarimetric unit U_R^y, having a $\pi/8$ tilt with respect to the [010] direction, one can observe strong dependence of the nonlinear response on the input SoP. Rotation of the periodic structure by the same angle, but in the opposite direction compared to U_R^y, i.e., $\beta = -\pi/8$, results in a map obtained through inversion about the point $(\chi, \psi) = (0, \pi/2)$, corresponding to the behavior of a U_L^y unit. In turn, units U_L^x and U_R^x, tilted with respect to the orthogonal [100] direction, demonstrate a $\pi/2$ shift along the ψ axis, compared to the corresponding maps of $U_{R,L}^y$ units. Left panel of Figure 2b shows the vertical slices of the maps ($\psi = 0$). Here one can see that $U_R^{x,y}$ units generate a negligibly small SH signal under LCP input ($\chi = -\pi/4$), with the signal increasing toward the RCP input ($\chi = \pi/4$). As expected, $U_L^{x,y}$ units feature the opposite dependence on the ellipticity angle. In case of linearly polarized input (Figure 2b, right panel, $\chi = 0$), the dependencies on the orientation angle ψ exhibit one maximum and one minimum for each value of the ellipticity angle, approximating shifted $\cos^2(\psi + \psi_0)$ dependence, showed by dashed lines. We observe that the SH-CD value monotonically decreases as the FF wavelength is shifted away from 1550 nm, at which it reaches its maximum, and drops to approximately 0.6 for a detuning of ± 100 nm (see Figure 2c). The nonlinear conversion efficiency of the unit can be described in terms of the nonlinear conversion coefficient $\xi^{2\omega} = P^{2\omega}/(P^{\omega})^2$, where $P^{2\omega}$ and P^{ω} is the power of the output SH and input FF radiation, respectively. From the numerical results shown in Figure 2, we

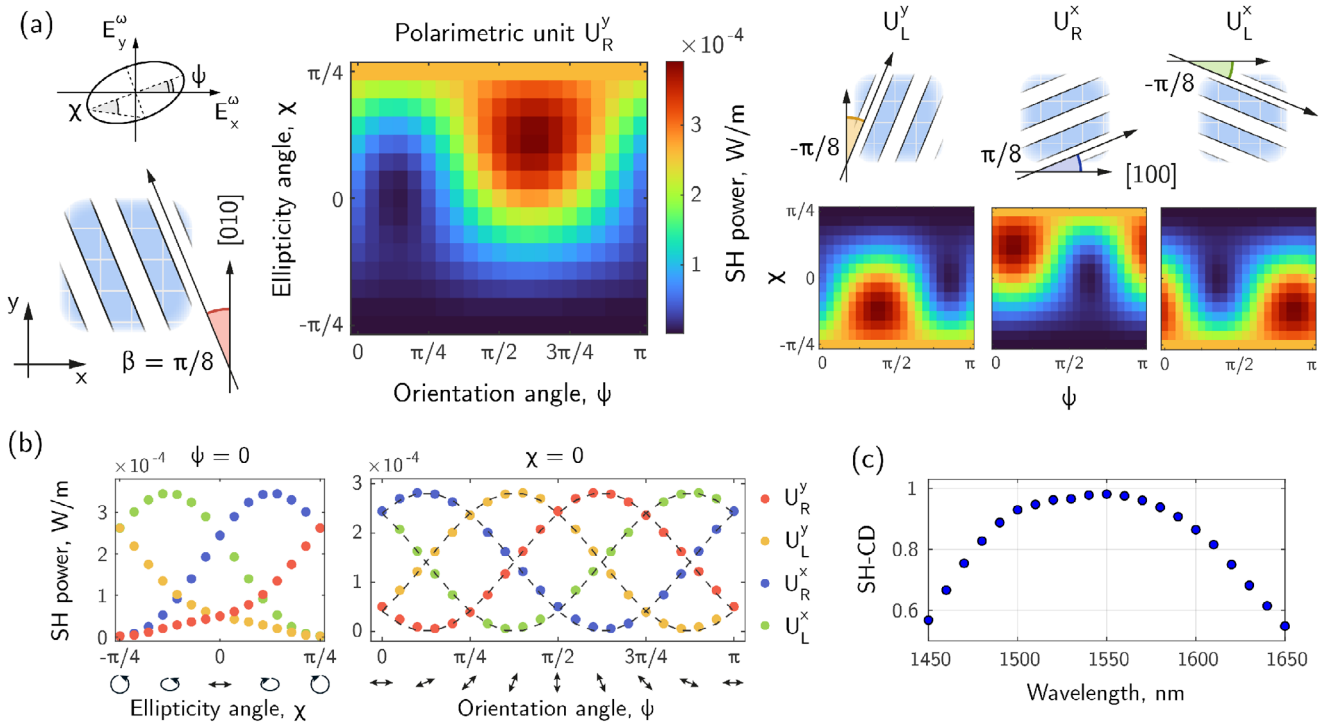

FIGURE 2 | Second harmonic response from the polarimetric units with input intensity $I_0^\omega = 1$ MW/cm^2. (a) SH map at 1550 nm for the U_R^y unit, rotated by the angle $\beta = \pi/8$ with respect to [010] direction (y-axis), as a function of the ellipticity and orientation angles of the polarization ellipse. Structure U_L^y ($\beta = -\pi/8$) features inverted map, showing the opposite dependence to the handedness of the input. (b) Dependence of SH signal power on the orientation angle ψ is similar to the response of a linear polarizer $I \propto \cos^2\psi$ depicted by dashed lines; colored markers correspond to slices of SH maps with $\psi = 0$ and $\chi = 0$. (c) Dependence of the nonlinear circular dichroism on the input wavelength features a maximum near 1550 nm.

obtain $\xi^{2\omega} \simeq 4 \times 10^{-9}$ W^{-1} (see Section S3.1 for more details). The efficiency value can be optimized, by specifically targeting high Q-factor optical resonances, allowing to increase the conversion efficiency of the process by several orders of magnitude [38–40]. We also note that the linear transmittance of the grating units shows relatively weak dependence on the orientation angle ψ, and is not sensitive to the handedness of the excitation, due to the nonchiral geometry (see Section S4).

2.2 | Analytical Analysis of Nonlinear Response

The analysis of the fields excited in the structures suggests that the nonlinear response induced by an input with arbitrary SoP can be expressed by a semi-analytical formula. Specifically, the generated SH field at position $\mathbf{r}$ can be written in terms of complex-valued vector parameters $\mathbf{E}_{AB}^{2\omega}$. These parameters represent the second harmonic electric field components generated by RCP and LCP photons, yielding four possible combinations: excitation by two RCP photons ($AB = RR$), two LCP photons (LL), and the cross terms arising from the combinations of RCP and LCP photons (RL, LR). This leads to the following response for excitation with an arbitrary SoP (see Appendix A.1 for details):

$$\mathbf{E}^{2\omega}(\mathbf{r}) = \left(\cos^2\frac{\theta}{2}\mathbf{E}_{RR}^{2\omega} + \cos\frac{\theta}{2}\sin\frac{\theta}{2}e^{-2i\psi}(\mathbf{E}_{RL}^{2\omega} + \mathbf{E}_{LR}^{2\omega}) + \sin^2\frac{\theta}{2}e^{-4i\psi}\mathbf{E}_{LL}^{2\omega}\right) \quad (1)$$

where $\theta/2 = -\chi + \pi/4$, with χ being the ellipticity angle. Notably, this formulation can be used to fully describe nonlinear vector response for an arbitrary SoP using only four numerical simulations, thus dramatically reducing the computational time required to characterize the system.

2.2.1 | Nonlinear Response Under Linearly Polarized Excitation

From analysis of Equation (1) we show that we show that structures with near unity SH-CD under linearly polarized excitation ($\chi = 0$) feature dependence of SH signal intensity approximated by the following equation (see Appendix A.2):

$$I^{2\omega} \approx a + b\cos(2\psi + \psi_0), \quad (2)$$

Fitting of the normalized calculated dependencies at 1550 nm gives for the coefficients a and b values of 0.507 and 0.489, respectively. Given the close values of the coefficients, Equation (2) can be rewritten as $I^{2\omega} \approx 2b\cos^2(\psi + \psi_0/2) + \varepsilon$, with $\varepsilon = a - b = 0.018$. Such behavior closely resembles the conventional dependence of light intensity transmitted through a rotated linear polarizer [41, 42]. We should note that while working in the region with near unity SH-CD approximately gives the $\cos^2(\psi)$ law, detuning from the optimized wavelength results in decreased SH-CD, changing the shape of the ψ dependence. We find that in the general case for our structure (including cases with the SH response of the same order for RCP and LCP excitation) the fitting

function includes an additional angular harmonic:

$$I^{2\omega} = a + b\cos(2\psi + \psi_b) + d\cos(4\psi + \psi_d), \tag{3}$$

where the relative weight of the coefficient d increases with detuning from the optimized wavelength. The results of the fit with Equation (3) are in perfect agreement with the numerical results (see Appendix A.2).

2.2.2 | Nonlinear Response Under Circularly Polarized Excitation

Next, we focus on the description of SH response under circularly polarized excitation. Periodic arrays of AlGaAs strips exhibit C_{2v} symmetry, for which the nonlinear polarization can be expressed in cylindrical coordinates (r, φ, z) as follows [36, 43]:

$$\mathbf{P}^{2\omega}_{m_{\text{in}}}(r,\varphi,z) \propto \sum_{\nu} e^{\mathrm{i}2\varphi\nu}\Big(\mathbf{P}^{2\omega}_{-2+2m_{\text{in}},\nu}(r,z)e^{\pm(-2+2m_{\text{in}})\mathrm{i}\varphi}e^{\pm 2\mathrm{i}\beta} + \mathbf{P}^{2\omega}_{2+2m_{\text{in}},\nu}(r,z)e^{\pm(2+2m_{\text{in}})\mathrm{i}\varphi}e^{\mp 2\mathrm{i}\beta}\Big) \tag{4}$$

where summation is over $\nu \in \mathbb{Z}$, β is the angle of the crystalline lattice rotation with respect to a vertical mirror plane, and m_{in} is the total angular momentum (TAM) projection of the incident wave on the propagation z-axis ($m_{\text{in}} = -1$ and $+1$ for RCP and LCP, respectively). The dependence of each term on φ corresponds to a TAM projection of the eigenmode, excited by this term. Basically, in C_{2v} structures there are only 4 types of eigenmodes: two of them have all possible even values of m and the other two have odd [44]. In our considerations, only eigenmodes with even m are excited by all $\mathbf{P}^{2\omega}_{m,\nu}$ terms. For orthogonal inputs ($m_{\text{in}} = \pm 1$) we can rewrite Equation (4) as follows:

$$\begin{aligned}\mathbf{P}^{2\omega}_{\text{L}}(r,\varphi,z) &\propto \sum_{\nu} e^{2\mathrm{i}\varphi\nu}\left(\mathbf{P}^{2\omega}_{0,\nu}(r,z) + \mathbf{P}^{2\omega}_{4,\nu}(r,z)e^{4\mathrm{i}\varphi}e^{-4\mathrm{i}\beta}\right)\\ \mathbf{P}^{2\omega}_{\text{R}}(r,\varphi,z) &\propto \sum_{\nu} e^{2\mathrm{i}\varphi\nu}\left(\mathbf{P}^{2\omega}_{0,\nu}(r,z) + \mathbf{P}^{2\omega}_{-4,\nu}(r,z)e^{-4\mathrm{i}\varphi}e^{4\mathrm{i}\beta}\right)\end{aligned} \tag{5}$$

Let us keep in mind that each polarization term then excites eigenmodes of the nanostructure of the corresponding symmetry. In order to qualitatively analyze the nonlinear CD, we can truncate the series to $\nu = 0$ terms, assuming that they provide the dominant contribution to the induced polarization. This approximation makes considerations simpler, and does not change the qualitative result. One can easily extend the analysis to higher-order terms, but the conditions for the dichroism will remain the same.

$$\begin{aligned}\mathbf{P}^{2\omega}_{\text{L}} &= \mathbf{P}_{0,0} + \left(\mathbf{P}_{4,0}e^{4\mathrm{i}\varphi}\right)e^{-4\mathrm{i}\beta}\\ \mathbf{P}^{2\omega}_{\text{R}} &= \mathbf{P}_{0,0} + \left(\mathbf{P}_{-4,0}e^{-4\mathrm{i}\varphi}\right)e^{4\mathrm{i}\beta}\end{aligned} \tag{6}$$

We note that, as the periodic structure is not chiral, modes excited by the polarization terms with $|\mathbf{P}^{2\omega}_{-4,0}|$ and $|\mathbf{P}^{2\omega}_{4,0}|$ with opposite TAM projections must have the same magnitude. In general, two terms excite eigenmodes of the same symmetry, but with different amplitudes. One can assume that $|\mathbf{P}^{2\omega}_{0,0}|$ excites one eigenmode, and $|\mathbf{P}^{2\omega}_{\pm 4,0}|$ another one, with different phase and amplitude. The phase difference between the modes excited by $m = 0$ term and terms with $m = \pm 4$ equals δ_{m}. Here, we also assumed that each term excites mostly one mode, while in reality both terms excite an infinite number of eigenmodes with different amplitudes. Also, for tilt angles $\beta \neq \frac{\pi\nu}{4} = 0, \pm 45°, \pm 90°, \ldots$, the exponential factors in Equation (6) do not coincide $e^{\mathrm{i}\delta_{\text{m}} - 4\mathrm{i}\beta} \neq e^{\mathrm{i}\delta_{\text{m}} + 4\mathrm{i}\beta}$. Therefore, we see that the magnitude of the total radiated power differs between LCP and RCP, enabling the chiral discrimination and the access to the S_3 component.

Also assuming the same absolute values of the amplitudes of the excited eigenmodes and integrating for the SH intensity [36] we obtain:

$$I^{2\omega} \propto (1 + \cos(\delta_{\text{m}} \mp 4\beta))^2 \tag{7}$$

where δ_{m} is the relative phase between the modes, determining the modulation depth of the SH-CD. Figure 2b (left panel) plots the total power as a function of the ellipticity angle. It can be seen that for U_R units as the angle varies from $-\pi/4$ (LCP) to $\pi/4$ (RCP), the intensity of the SH signal gradually increases from approximately zero to its nominal value.

3 | Stokes Parameters Retrieval and Performance Estimation

After describing the properties of the nonlinear response of the individual units, we will now discuss how the distinct SH dependencies of a polarimetric super-pixel (or a set of four dielectric polarimetric units) allow to connect the intensities of the SH signal with the polarization state of the input light. First, we consider the procedure allowing for the retrieval of the polarization state from measured SH power. Next, we show that the response of the units allows for full Stokes polarimetry of fully polarized light using a LUT approach, described below. The retrieval capabilities of the proposed method are reported in Figure 3, where the representation of the SoP under analysis is described as a point located on the Poincaré sphere [1]. We note that the nonlinear device enables polarimetric measurements of partially polarized light (i.e., full Stokes polarimetry), for which we propose an alternative approach detailed in Section S7.

3.1 | Stokes Parameters Retrieval With Fully Polarized Input

To retrieve the Stokes parameters of the input signal, we create a set of lookup tables (LUTs), $T_i(\psi, \chi)$, of size 21×11 ($\psi \times \chi$), containing the SH power for the corresponding polarization states with fully polarized input. Values between the calculated points are evaluated using linear interpolation. A LUT is calculated for each polarimetric unit at specified input signal intensities and wavelengths. Given the quadratic dependence of the generated SH signal, we assume that the value of the measured SH power, p_i, can be obtained by scaling the values taken from the LUTs:

$$p'_i = \left(\frac{I}{I_c}\right)^2 T_i(\psi, \chi) \tag{8}$$

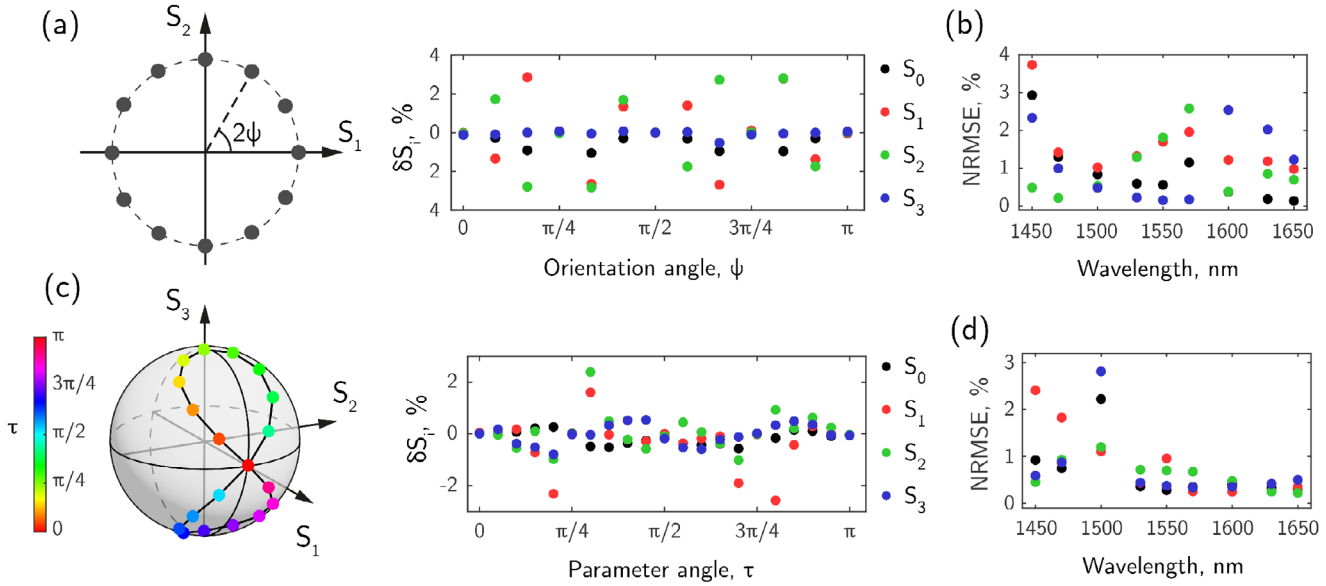

FIGURE 3 | Stokes parameters retrieval from the second harmonic signal intensity measurements. (a) Reference input of the tested linear SoPs displayed on the Poincaré sphere (left panel) and the error of the retrieved Stokes parameters at input wavelength of 1550 nm (right panel). (b) Dependence of the normalized RMSE on the wavelength of linearly polarized input light. (c) Polarization states produced by a quarter-wave plate rotated by an angle τ (left panel), and the corresponding retrieval error (right panel). (d) Dependence of the normalized RMSE on the wavelength of the input light.

where p_i' is the expected SH power from i-th structure, I is the input intensity, I_c is the intensity at which the LUT (T_i) was calculated. With this assumption, we optimize the polarization ellipse angles and the input intensity by minimizing the difference between the scaled LUT values and the measured SH power from each element:

$$\min_{I>0,\psi,\chi} \|(\mathbf{p} - \alpha\,\mathbf{T}(\psi,\chi))\|^2, \qquad \alpha = \left(\frac{I}{I_c}\right)^2, \tag{9}$$

$$\text{with} \quad \mathbf{p} = [p_1, p_2, p_3, p_4], \quad \mathbf{T} = [T_1, T_2, T_3, T_4].$$

The minimization was performed using a simulated annealing algorithm. In order to estimate the accuracy of the retrieval we introduce the retrieval error defined as follows:

$$\delta S_i = \frac{S_i^{\text{fit}} - S_i^{\text{in}}}{S_0^{\text{in}}} \tag{10}$$

where S_i^{fit} is the i-th Stokes parameter obtained during the optimization procedure, and S_i^{in} is the parameter corresponding to the SoP of the input. In order to estimate average error for a set of points obtained with the same input intensity $I_{\text{in}}^{\omega} = S_0^{\text{in}}$, we use the normalized root mean square error (NRMSE) defined as:

$$\text{NRMSE}_i = \frac{1}{S_0^{\text{in}}} \sqrt{\frac{1}{N}\sum_{n=1}^{N} \left(S_i^{\text{fit}}(n) - S_i^{\text{in}}(n)\right)^2} \tag{11}$$

3.1.1 | Linear Input Polarization States

Figure 3a illustrates the set of SoPs for linearly polarized input, represented by points on the equator of the Poincaré sphere ($\chi = 0$), together with the error of the retrieved Stokes parameters at an input wavelength of 1550 nm. Here, during optimization, we did not enforce $\chi = 0$, allowing the algorithm to retrieve all Stokes parameters. We observe that in this case the absolute error is less than 4%. Notably, for points with ψ equal to integer multipliers of $\pi/4$, the error drops to near zero values compared to neighboring points. This can be attributed to the overlap between the points from the test set and the values from the LUTs, whereas the neighboring test points correspond to linearly interpolated LUT values. Figure 3b shows the normalized RMSE a s function of the input wavelength, showing that in the whole range of wavelengths the NRMSE does not exceed 4%.

3.1.2 | Elliptical Input Polarization States

Next, we focus on full perform Stokes polarimetry using another test set of polarization states, which can be produced experimentally by passing a linearly polarized beam through a rotating quarter-wave plate (QWP) (see Section S5). In this case the trajectory of the input SoP forms on the sphere a lemniscate like shape (see Figure 3c, left panel) parametrized by the QWP rotation angle τ. When the fast axis of QWP is aligned with the input polarization ($\tau = 0$), the input state remains unchanged, while at $\tau = \pi/4$, the waveplate transforms the linear input into circularly polarized one. The right panel of Figure 3c presents the error of the retrieved Stokes parameters at 1550 nm, showing that the absolute error does not exceed 2%. The normalized RMSE for retrieval in the wavelength range 1450–1650 nm remains below 3%, as shown in Figure 3d.

3.2 | Performance Estimation

Finally, regarding the realization of the proposed device, we provide an estimation for the threshold value of the input power

at fundamental frequency required for the operation (see Section S3.2 for more details). For this purpose, we consider a CCD camera featuring a maximum well capacity of 23 000 electrons, an efficiency of $\epsilon \sim 40\%$ at $\lambda_{SH} = 775$ nm (which corresponds to the SH of a FF beam at 1550 nm), and a pixel size of $p \sim 5$ μm (e.g., Thorlabs CS2100-USB). Moreover, we consider the polarimetric unit consisting in a grating structure covering a square region with area $A_u = LN\Lambda$, where L is the bar length and N the number of bars within the polarimetric unit. Given a value of $\xi^{2\omega} \simeq 4 \times 10^{-9}$ W^{-1} for $L = 25$ μm and $N = 19$, in order to excite $N_e = 2000$ electrons in a time interval $\Delta t = 5$ s in the case of a single pixel, the required intensity of the pulsed FF excitation can be estimated as

$$I_m^{\omega} = I_0^{\omega} \sqrt{\frac{RR\tau\, 2\pi\hbar c N_e}{\tilde{P}_0^{2\omega} LN\epsilon\, \Delta t\, \lambda_{SH}}} = 23\ \text{mW/cm}^2, \tag{12}$$

where the pulse duration $\tau = 300$ fs and the repetition rate $RR = 1$ MHz. We underline that this estimation is based on the assumption that each single analyzer pixel (comprising one polarimetric unit) is imaged onto one single detector pixel.

4 | Conclusions

In this work, we presented a novel approach to polarimetric imaging based on second-harmonic generation in nonlinear flat-optics platform. By exploiting the polarization dependence of the nonlinear response in $\chi^{(2)}$ nonlinear crystal of AlGaAs, and by optimizing the geometrical parameters of dielectric gratings, we demonstrated that the intensity of the generated SH signal encodes the full state of polarization of the FF incident light. We analytically analyzed the observed dependencies, revealing the relation between the absolute value of SH dichroism and the shape of the response to the polarization orientation angle.

Through numerical simulations, we showed that four identical elements with simple geometry, can serve as micropolarizers of both linear and circular polarizations, selectively enhancing or suppressing SH signals based on the input polarization state. By assembling four such elements into super-pixel arrays, we proposed a complete polarization analyzer capable of retrieving all four Stokes parameters from a single image capture of the SH intensity distribution. We find that such a device can operate with high accuracy (error $< 4\%$) in a wide range of wavelengths spanning from 1450 to 1650 nm.

Our findings indicate that nonlinear harmonic generation offers a promising route to compact, passive, and cost-effective polarimetric imaging systems.

Acknowledgements

The authors are thankful to Rinaldo Colombo, Mercedeh Khajavikhan, Giuseppe Leo, Michele Midrio, Luca Palmieri, and Luca Schenato for fruitful discussions. This work was partially supported by the European Union under the Italian National Recovery and Resilience Plan (NRRP) of NextGenerationEU, of partnership on "Telecommunications of the Future" (PE00000001 - program "RESTART"), Cascade project PRISM - CUP: C79J24000190004, Cascade project SMART - CUP: E63C22002040007, Smart Metasurfaces Advancing Radio Technology (SMART), PRIN 2020 project METEOR (2020EY2LJT), METAFAST project that received funding from the European Union Horizon 2020 Research and Innovation programme under Grant Agreement No. 899673. A. T. acknowledges the financial support from the University of Palermo through "Fondo Finalizzato alla Ricerca di Ateneo 2025 (FFR2025)". K.F. gratefully acknowledges support from the Alexander von Humboldt Foundation.

Open access publishing facilitated by Universita degli Studi di Brescia, as part of the Wiley - CRUI-CARE agreement.

Conflicts of Interest

The authors declare no conflicts of interest.

Data Availability Statement

The data that support the findings of this study are available from the corresponding author upon reasonable request.

References

1. M. Born and E. Wolf, *Principles of Optics*, 6th ed (Pergamon Press, 1980).

2. N. A. Rubin, Z. Shi, and F. Capasso, "Polarization in Diffractive Optics and Metasurfaces," *Advances in Optics and Photonics* 13, no. 4 (2022): 836–970.

3. J. S. Tyo, D. L. Goldstein, D. B. Chenault, and J. A. Shaw, "Review of Passive Imaging Polarimetry for Remote Sensing Applications," *Applied Optics* 45, no. 22 (2006): 5453–5469, https://opg.optica.org/ao/abstract.cfm?URI=ao-45-22-5453.

4. D. V. Cotton, J. Bailey, I. D. Howarth, et al., "Polarization Due to Rotational Distortion in the Bright Star Regulus," *Nature Astronomy* 1 (2006): 690.

5. P. Lodahl, S. Mahmoodian, S. Stobbe, et al., "Chiral Quantum Optics," *Nature* 541 (2017): 473.

6. N. Ghosh and I. A. Vitkin, "Tissue Polarimetry: Concepts, Challenges, Applications, and Outlook," *Journal of Biomedical Optics* 16, no. 11 (2011): 110 801–110 801.

7. N. M. Garcia, I. De Erausquin, C. Edmiston, and V. Gruev, "Surface Normal Reconstruction Using Circularly Polarized Light," *Optics Express* 23, no. 11 (2015): 14391–14406.

8. O. Morel, C. Stolz, F. Meriaudeau, and P. Gorria, "Active Lighting Applied to Three-Dimensional Reconstruction of Specular Metallic Surfaces by Polarization Imaging," *Applied Optics* 45, no. 17 (2006): 4062–4068.

9. G. A. Atkinson and E. R. Hancock, "Recovery of Surface Orientation from Diffuse Polarization," *IEEE Transactions on Image Processing* 15, no. 6 (2006): 1653–1664.

10. M. Malinowski, A. Gilerson, E. Herrera-Estrella, and J. Agagliate, "Polarimetric Imaging of the Ocean Surface for the Study of Ocean Surface Roughness and Wave Slopes Statistics," in *Ocean Sensing and Monitoring XV*, vol. 12543 (SPIE, 2023), 214–225.

11. Y. Shkuratov, N. Opanasenko, E. Zubko, et al., "Multispectral Polarimetry as a Tool to Investigate Texture and Chemistry of Lunar Regolith Particles," *Icarus* 187, no. 2 (2007): 406–416.

12. S. Brasselet and M. A. Alonso, "Polarization Microscopy: From Ensemble Structural Imaging to Single-Molecule 3D Orientation and Localization Microscopy," *Optica* 10, no. 11 (2023): 1486–1510.

13. J. Kim, R. Chacón, Z. Wang, et al., "Measuring 3D Orientation of Nanocrystals via Polarized Luminescence of Rare-Earth Dopants," *Nature Communications* 12, no. 1 (2021): 1943.

14. E. Bruggeman, O. Zhang, L.-M. Needham, et al., "POLCAM: Instant Molecular Orientation Microscopy for the Life Sciences," *Nature Methods* 21 (2024): 1873–1883, https://www.nature.com/articles/s41592-024-02382-8.

15. J. A. Schellman, "Circular Dichroism and Optical Rotation," *Chemical Reviews* 75, no. 3 (1975): 323–331.

16. B. Schaefer, E. Collett, R. Smyth, D. Barrett, and B. Fraher, "Measuring the Stokes Polarization Parameters," *American Journal of Physics* 75, no. 2 (2007): 163–168.

17. E. Compain and B. Drevillon, "Broadband Division-of-Amplitude Polarimeter Based on Uncoated Prisms," *Applied Optics* 37, no. 25 (1998): 5938–5944.

18. L. Wolff, T. Mancini, P. Pouliquen, and A. Andreou, "Liquid Crystal Polarization Camera," *IEEE Transactions on Robotics and Automation* 13, no. 2 (1997): 195–203.

19. A. D. Martino, Y.-K. Kim, E. Garcia-Caurel, B. Laude, and B. Drévillon, "Optimized Mueller Polarimeter with Liquid Crystals," *Optics Letters* 28, no. 8 (2003): 616–618.

20. J. Guo and D. Brady, "Fabrication of Thin-Film Micropolarizer Arrays for Visible Imaging Polarimetry," *Applied Optics* 39, no. 10 (2000): 1486–1492.

21. V. Gruev, A. Ortu, N. Lazarus, J. V. der Spiegel, and N. Engheta, "Fabrication of a Dual-Tier Thin Film Micropolarization Array," *Optics Express* 15, no. 8 (2007): 4994–5007, https://opg.optica.org/oe/abstract.cfm?URI=oe-15-8-4994.

22. H. Yuan, X. Liu, F. Afshinmanesh, et al., "Polarization-Sensitive Broadband Photodetector Using a Black Phosphorus Vertical P–N Junction," *Nature Nanotechnology* 10, no. 8 (2015): 707–713.

23. Y. Fan, J. Chu, R. Zhang, et al., "Broadband Visible–Near-Infrared Circular Polarizer with Cascaded Aluminum Wire-Grid," *Advanced Materials Technologies* 8, no. 7 (2023): 2201394.

24. K. Bachman, J. Peltzer, P. Flammer, T. Furtak, R. Collins, and R. Hollingsworth, "Spiral Plasmonic Nanoantennas as Circular Polarization Transmission Filters," *Optics Express* 20, no. 2 (2012): 1308–1319.

25. Y. Zhang, J. Wu, L. Jia, et al., "Advanced Optical Polarizers Based on 2D Materials," *npj Nanophotonics* 1, no. 1 (2024): 28.

26. N. Yu, P. Genevet, M. A. Kats, et al., "Light Propagation with Phase Discontinuities: Generalized Laws of Reflection and Refraction," *Science* 334, no. 6054 (2011): 333–337.

27. N. Yu and F. Capasso, "Flat Optics with Designer Metasurfaces," *Nature Materials* 13 (2014): 139.

28. P. Lalanne, S. Astilean, P. Chavel, E. Cambril, and H. Launois, "Blazed Binary Subwavelength Gratings with Efficiencies Larger Than Those of Conventional Échelette Gratings," *Optics Letters* 23, no. 14 (1998): 1081–1083.

29. E. Arbabi, S. M. Kamali, A. Arbabi, and A. Faraon, "Full-Stokes Imaging Polarimetry Using Dielectric Metasurfaces," *ACS Photonics* 5 (2018): 3132.

30. N. A. Rubin, G. D'Aversa, P. Chevalier, Z. Shi, W. T. Chen, and F. Capasso, "Matrix Fourier Optics Enables a Compact Full-Stokes Polarization Camera," *Science* 365, no. 6448 (2019): eaax1839.

31. Y. Intaravanne and X. Chen, "Recent Advances in Optical Metasurfaces for Polarization Detection and Engineered Polarization Profiles," *Nanophotonics* 9, no. 5 (2020): 1003–1014.

32. L. Li, J. Wang, L. Kang, et al., "Monolithic Full-Stokes Near-Infrared Polarimetry with Chiral Plasmonic Metasurface Integrated Graphene–Silicon Photodetector," *ACS Nano* 14 (2020): 16634.

33. F. Tian, Y. Jia, H. Luo, et al., "Weyl Semimetal Integrated Three-Unit Polarimeters," *Optica* 9, no. 10 (2022): 1115–1120.

34. J. Zuo, J. Bai, S. Choi, et al., "Chip-Integrated Metasurface Full-Stokes Polarimetric Imaging Sensor," *Light: Science and Applications* 12, no. 1 (2023): 218.

35. L. Carletti, D. Rocco, M. A. Vincenti, D. de Ceglia, and C. D. Angelis, "Intrinsic Nonlinear Geometric Phase in SHG from Zincblende Crystal Symmetry Media," *Nanophotonics* 13, no. 18 (2024): 3321–3326, https://doi.org/10.1515/nanoph-2024-0162.

36. A. Nikitina and K. Frizyuk, "Achiral Nanostructures: Perturbative Harmonic Generation and Dichroism Under Vortex and Vector Beams Illumination," *Advanced Optical Materials* 12, no. 25 (2024): 2400732.

37. W.-L. Hsu, G. Myhre, K. Balakrishnan, N. Brock, M. Ibn-Elhaj, and S. Pau, "Full-Stokes Imaging Polarimeter Using an Array of Elliptical Polarizer," *Optics Express* 22, no. 3 (2014): 3063–3074.

38. N. Bernhardt, K. Koshelev, S. J. U. White, et al., "Quasi-BIC Resonant Enhancement of Second-Harmonic Generation in WS2 Monolayers," *Nano Letters* 20, no. 7 (2020): 5309–5314, https://doi.org/10.1021/acs.nanolett.0c01603.

39. L. Carletti, K. Koshelev, C. De Angelis, and Y. Kivshar, "Giant Nonlinear Response at the Nanoscale Driven by Bound States in the Continuum," *Physical Review Letters* 121, no. 3 (2018): 033903, https://link.aps.org/doi/10.1103/PhysRevLett.121.033903.

40. P. Franceschini, A. Tognazzi, E. Menshikov, et al., "Intrapulse Multimodal Four-Wave Sum Mixing in the Visible Range from High Contrast Index Grating with PMMA Layer," *Light: Science and Applications* 15, no. 51 (2026): 51, https://www.nature.com/articles/s41377-025-02090-8.

41. D. de Ceglia, M. A. Vincenti, C. D. Angelis, A. Locatelli, J. W. Haus, and M. Scalora, "Role of Antenna Modes and Field Enhancement in Second Harmonic Generation from Dipole Nanoantennas," *Optics Express* 23, no. 2 (2015): 1715–1729, https://opg.optica.org/oe/abstract.cfm?URI=oe-23-2-1715.

42. E. Collett, "Polarized Light: Fundamentals and Applications," *Optical Engineering* (1992), https://ui.adsabs.harvard.edu/abs/1992plfa.book...C/abstract.

43. A. Nikitina, A. Nikolaeva, and K. Frizyuk, "Nonlinear Circular Dichroism in Achiral Dielectric Nanoparticles," *Physical Review B* 107, no. 4 (2023): L041405, https://doi.org/10.1103/PhysRevB.107.L041405.

44. S. Gladyshev, K. Frizyuk, and A. Bogdanov, "Symmetry Analysis and Multipole Classification of Eigenmodes in Electromagnetic Resonators for Engineering Their Optical Properties," *Physical Review B* 102, no. 7 (2020): 075103, https://doi.org/10.1103/PhysRevB.102.075103.

45. L. Freter, B. Zerulla, M. Krstić, C. Holzer, C. Rockstuhl, and I. Fernandez-Corbaton, "Tensor Product Space for Studying the Interaction of Bipartite States of Light with Nanostructures," *Physical Review A* 110, no. 4 (2024): 043516, https://doi.org/10.1103/PhysRevA.110.043516.

46. K. Koshelev, I. Toftul, Y. Hwang, and Y. Kivshar, "Scattering Matrix for Chiral Harmonic Generation and Frequency Mixing in Nonlinear Metasurfaces," *Journal of Optics* 26, no. 5 (2024): 055003, https://doi.org/10.1088/2040-8986/ad3a78.

47. K. Frizyuk, I. Volkovskaya, D. Smirnova, A. Poddubny, and M. Petrov, "Second-Harmonic Generation in Mie-Resonant Dielectric Nanoparticles Made of Noncentrosymmetric Materials," *Physical Review B* 99, no. 7 (2019): 075425, https://doi.org/10.1103/PhysRevB.99.075425.

Supporting Information

Additional supporting information can be found online in the Supporting Information section.

Supporting File: lpor71289-sup-0001-SuppMat.pdf.

Appendix A

A.1 | Functional Dependence on the Incident Polarization

In this section, we provide an analytical description of our system, offering valuable insights into the underlying physics. Let us denote incident left(right)-circularly polarized plane wave as $|L\rangle$ ($|R\rangle$), or more generally, a beam with TAM projection $m_{\text{in}} = -1(+1)$. In this basis, the SoP of an arbitrarily polarized input wave $|E^{\omega}\rangle$ can then be expressed as

$$|E^{\omega}\rangle \propto \left(\cos\frac{\theta}{2}e^{i\psi}\,|R\rangle + \sin\frac{\theta}{2}e^{-i\psi}\,|L\rangle\right) \sim \left(\cos\frac{\theta}{2}\,|R\rangle + \sin\frac{\theta}{2}e^{-2i\psi}\,|L\rangle\right) \tag{A1}$$

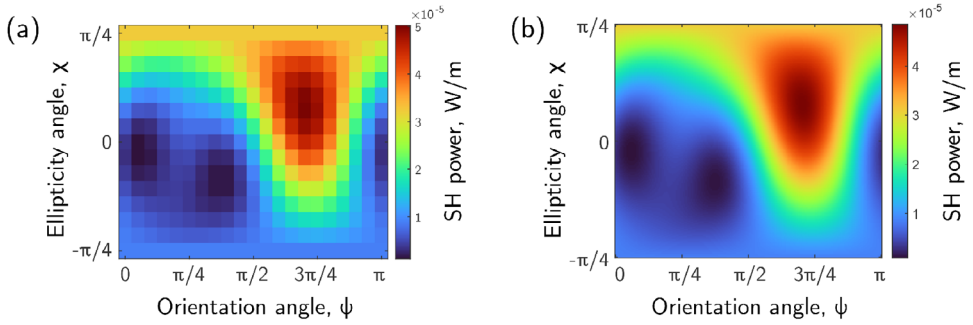

FIGURE A1 | Maps of SH response from U_R^y polarimetric unit at 1450 nm. (a) Numerical calculation for each input SoP, (b) semil-analytical approach expressed by Equation (A4).

The equivalence sign $\sim$ is used, because for these two formulae describe the same polarization state, as long as we are not interested in the total phase, but still care about the amplitude, to compare the SH responses to different polarizations. We can then describe the input for the SHG process as the tensor product of the incident wave [36, 45, 46], i.e. $|E^{\omega}\rangle \otimes |E^{\omega}\rangle$. Let us denote the whole process of SHG by $\mathcal{F}$, because, in this consideration, we are not interested in particular properties of this process. The second harmonic field $\mathbf{E}^{2\omega}(\mathbf{r})$ can then be written as

$$\begin{aligned}\mathbf{E}^{2\omega}(\mathbf{r}) &= \mathcal{F}(\mathbf{r})(|E\rangle \otimes |E\rangle) = \\ &= \mathcal{F}(\mathbf{r})\left(\left(\cos\frac{\theta}{2}|R\rangle + \sin\frac{\theta}{2}e^{-2i\psi}|L\rangle\right)\right. \\ &\left.\otimes\left(\cos\frac{\theta}{2}|R\rangle + \sin\frac{\theta}{2}e^{-2i\psi}|L\rangle\right)\right) = \\ &= \mathcal{F}(\mathbf{r})\left(\cos^2\frac{\theta}{2}|R\rangle\otimes|R\rangle + \cos\frac{\theta}{2}\sin\frac{\theta}{2}e^{-2i\psi}(|L\rangle\otimes|R\rangle\right. \\ &\left. + \ |R\rangle\otimes|L\rangle) + \sin^2\frac{\theta}{2}e^{-4i\psi}|L\rangle\otimes|L\rangle\right)\end{aligned} \tag{A2}$$

The question arises: is $\mathcal{F}(\mathbf{r})$ linear? First, the fields undergo linear scattering. Fields inside the nanostructure do not possess the same shape as for plane wave, but importantly, the scattering process is linear. If the incident field is represented as a sum of two waves, the internal field is likewise represented as a sum of the internal fields generated by these two waves. We now consider the action of the second-order susceptibility $\chi^{(2)}$, which is nonlinear in the usual sense. However, when expressed in the tensor-product formalism as in Equation (A2), the corresponding operator acts linearly on the tensor-product space. The nonlinear polarization then generates the second-harmonic field, which can also be described linearly through Green's functions. Specifically, for any input $|E_i\rangle$, the output is expressed as $\mathcal{F}(\mathbf{r})(|E_1\rangle \otimes |E_2\rangle + |E_3\rangle \otimes |E_4\rangle) = \mathcal{F}(\mathbf{r})\,|E_1\rangle \otimes |E_2\rangle + \mathcal{F}(\mathbf{r})\,|E_3\rangle \otimes |E_4\rangle$.

Let us now introduce the notation for each term in Equation (A2) of the form:

$$\mathcal{F}(\mathbf{r})(|A\rangle \otimes |B\rangle) = \mathbf{E}_{AB}^{2\omega}. \tag{A3}$$

where A and B take values from the set $\{R, L\}$. Rewriting Equation (A2), we obtain the expression

$$\mathbf{E}^{2\omega}(\mathbf{r}) = \left(\cos^2\frac{\theta}{2}\mathbf{E}_{RR}^{2\omega} + \cos\frac{\theta}{2}\sin\frac{\theta}{2}e^{-2i\psi}(\mathbf{E}_{RL}^{2\omega} + \mathbf{E}_{LR}^{2\omega}) + \sin^2\frac{\theta}{2}e^{-4i\psi}\mathbf{E}_{LL}^{2\omega}\right) \tag{A4}$$

This is the second-harmonic electric field at some point $\mathbf{r}$ (an analogous expression holds for $\mathbf{H}^{2\omega}(\mathbf{r})$). To obtain the total SH intensity, one must calculate the local intensity by taking the square of the absolute value of the field and then integrate it over space. The subtle part is that each $\mathbf{E}_{AB}^{2\omega}$ is a vector quantity depending on the coordinate, and determining it requires additional calculations. However, we can look at the symmetry behavior of each of these terms [36], and immediately determine whether they interfere in the intensity, or not. They do interfere, if they possess at least partially coinciding values of total angular momentum projections m. This rule is applicable almost always, except for very specific cases, however, to be sure, one may also consider all the parities [47]. In our case, the nanostructure is of C_{2v} symmetry with GaAs tensor [001]||z, so each of the 4 terms generates all possible even m values. This means that all these partial SH-fields have the same symmetry behavior and interfere. Figure A1 shows SH response maps for the U_R^y unit at 1450 nm, obtained from explicit calculations for each input SoP and from Equation (A4) using only four simulations. One can observe close agreement between the semi-analytical results and the fully numerical calculations.

A.2 | Dependence of the Response With Linearly Polarized Input

Let us now focus on a specific case of linearly polarized input wave ($\theta = \pi/2$) incident on a structure with unity SH circular dichroism. This means, that one of the responses at SH, $\mathbf{E}_{RR}^{2\omega}$ or $\mathbf{E}_{LL}^{2\omega}$, is zero. Let us consider $\mathbf{E}_{LL}^{2\omega} = 0$. Values of $\mathbf{E}_{RL}^{2\omega}$ and $\mathbf{E}_{LR}^{2\omega}$ are not known, but let us assume that they are comparable to $\mathbf{E}_{RR}^{2\omega}$. In this case from Equation (A4) we get the expression in the following form:

$$\begin{aligned}P^{2\omega} &\propto \int |a(\mathbf{r}) + e^{-i2\psi}b(\mathbf{r})|^2 d\mathbf{r} \\ &= \int \left(|a(\mathbf{r})|^2 + |b(\mathbf{r})|^2 + 2|a(\mathbf{r})||b(\mathbf{r})|\cos(\delta(\mathbf{r}) - 2\psi)\right)d\mathbf{r}\end{aligned} \tag{A5}$$

and in principle we can assume the phase difference $\delta(\mathbf{r})$ between the fields close to constant (which is quite natural for the far-field of two interfering fields with the same m), getting the final expression (as in Equation 2) for the dependence on ψ:

$$I^{2\omega} \propto a + b\cos(2\psi + \psi_b) \tag{A6}$$

In the case of imperfect SH circular dichroism (comparable response from both $\mathbf{E}_{RR}^{2\omega}$ and $\mathbf{E}_{LL}^{2\omega}$ terms), integration of Equation (A4) gives:

$$I^{2\omega} \propto a + b\cos(2\psi + \psi_b) + d\cos(4\psi + \psi_d). \tag{A7}$$

Figure A2 shows the numerically calculated dependencies of SH power under linearly polarized excitation on the orientation angle calculated at various wavelengths (colored markers). Here we also provide fits of the calculated dependencies with the expressions (A6) and (A7), showed by dashed and solid lines, respectively. We find that the dependence at 1550 nm with SH-CD = 0.98, closely follows Equation (A6). In this case, the use of the more accurate expression (A7) does not significantly improve the accuracy of the fit, which is consistent with the derivation assumptions of

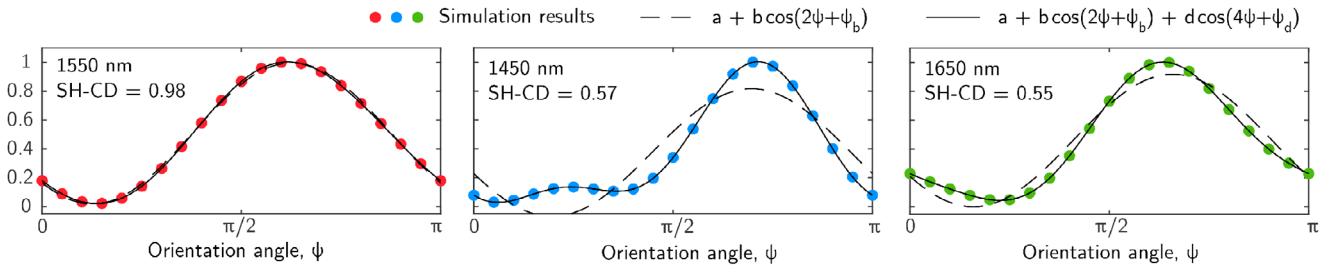

FIGURE A2 | Dependencies of the normalized SH power generated by the polarimetric unit on the orientation angle for an ellipticity angle $\chi = 0$. For small SH-CD values, the angular dependence becomes distorted due to the appearance of an additional harmonic. The simulated data and corresponding fits are shown by markers and lines, respectively.

TABLE A1 | Fitted parameters for three input wavelengths using simplified and extended formulations.

λ_{in}, nm	Model	a	b	ψ_b, rad.	d	ψ_d, rad.
1550	Simplified	0.5067	0.4892	2.3475	—	—
	Extended	0.5060	0.4902	2.3497	0.01763	−0.3081
1650	Simplified	0.4593	0.4597	2.1451	—	—
	Extended	0.4583	0.4608	2.1488	0.09605	−1.3270
1450	Simplified	0.3733	0.4431	1.9062	—	—
	Extended	0.3808	0.4384	1.8742	0.18610	−2.7527

near-unity CD. For input wavelengths of 1450 and 1650 nm (with SH-CD of 0.57 and 0.55 respectively), Equation (A6) fails to describe the observed dependence, resulting in a relatively large error, whereas Equation (A7) provides an excellent fit. Table A1 shows the fitting coefficients for the two expressions.